Neighbor-induced unsteady force in the interaction of a cylindrical shock wave with an annular particle cloud

Sam Briney [1], Andreas N. Osnes [2], Magnus Vartdal [2],
Thomas L. Jackson [1], and S. Balachandar [1]

[1]*Department of Mechanical and Aerospace Engineering, University of Florida, Gainesville, Florida 32611-6250, USA*
[2]*Norwegian Defense Research Establishment, P.O. Box 25, Kjeller 2007, Norway*

Multiphase volume-fraction-dependent quasisteady force models have recently been developed. These models account for the mean force on a particle in the presence of neighboring particles. Additionally, in shock-particle interaction, there is an unsteady effect to the perturbation flow induced by the neighbors and their arrival to a particle. Namely, there is an unsteady component to the volume fraction effect. The present work advances a simple model to capture this time-dependent perturbative influence of neighbors in the context of a shock propagating through a cloud of particles. This model makes use of existing quasisteady force correlations that account for volume fraction within the framework of the compressible Maxey-Riley-Gatignol equation. This new unsteady neighbor force is applied via a time history kernel. The problem is examined in the context of a shock propagating outward in cylindrical geometry. It is observed that for the radii of curvatures examined, the model prediction is accurate in recovering the time history of force and time-integrated impulse on the particles. By comparing with a classical model, we also highlight the importance of volume fraction correction in accurately extracting the long-time force and the importance of unsteady contribution in accurately predicting the peak shock-induced force.

I. INTRODUCTION

Force modeling on particles in the context of multiphase flow has a rich history extending over a century [1,2]. Many advancements have been made including in the Stokes regime, the incompressible regime, the compressible regime, and the noncontinuum regime [3–11]. Continuous improvement of these force models will result in more accurate Euler-Lagrange (EL) and Euler-Euler (EE) simulations of mesoscale and macroscale phenomena that are of relevance in numerous applied contexts. For instance, despite its importance in national security and industrial relevance [12,13], the problem of multiphase instabilities in an explosive dispersal of particles in cylindrical and spherical geometries is not well understood. These instabilities are fundamental and exist in the incompressible limit [14] as well as in strongly compressible flows [15,16]. Improvement of drag models will unlock a better understanding of such emergent mesoscale and macroscale effects.

The volume fraction effect due to fluid-mediated particle-particle interactions is significant in many applications where the distribution of particles is far from dilute. Volume-fraction-dependent drag correlations are actively being considered in the quasisteady (QS) regime and for uniform random distributions of particles [10,11,17–19]. However, volume fraction effects remain largely unexplored under unsteady and other complex conditions. In the quasisteady limit, investigations have revealed that the force on individual particles within random distributions is highly dependent on the microstructure of the neighboring particles in compressible flows [20,21] in ways more

complex than in incompressible flow [19,22,23] due to propagation of compression and rarefaction waves.

Here we examine the effect of volume fraction in the context of a shock expanding in cylindrical geometry through a cloud of particles. The corresponding problem of a planar shock propagating over a curtain of particles has been the subject of considerable research over the course of the past decade [20,24–31]. Some of these investigations examined shock-particle interactions at the level of individual particles with the aim of developing better closure models through improved fundamental understanding. The interest here is to extend this understanding to the closely related problem of a cylindrically expanding shock propagating through an annular bed of particles.

There are two main reasons for using cylindrical geometry for this work instead of planar geometry. First, it demonstrates decisively that the force models used in the planar configuration can be used in expanding geometry which is closer to practical applications [15,16,32–37]. Second, and more importantly, it allows us to consider a wider range of flow parameters since the shock strength decays due to curvature as it passes through the particle cloud. Therefore, the force models can be evaluated over a wider continuous range of shock Mach numbers using cylindrical geometry than would be possible using a planar configuration. Here we endeavor to understand and improve the force models to be used in EL simulations with a focus on volume fraction effects.

In particular, in this work, we explore a hitherto unexplored effect of volume fraction on unsteady force on particles, in the context of compressible flows. Under steady conditions, the effect of local volume fraction on the mean force on particles should be interpreted as the average influence of all the neighboring particles, including those upstream, downstream, and to the side. In contrast, consider the unsteady situation of shock propagation. When the shock arrives at a particle (referred to as the reference particle), it is influenced only by those neighbors that are directly upstream. During the early time, soon after the shock arrival at the reference particle, its downstream neighbors are still immersed in quiescent preshock fluid and their presence is not yet felt. Only when the shock has propagated sufficiently downstream of the reference particle will the perturbations from the downstream neighbors arrive at the reference particle. In other words, the full effect of local volume fraction, i.e., the effect of all the neighbors, is felt in a delayed fashion. We term this the unsteady neighbor effect, which will be an important focus of this work.

In this work, force prediction is pursued in the framework of the compressible version of the Maxey-Riley-Gatignol (C-MRG) equation [38,39], which encapsulates the time history of the force evolution in detail. The C-MRG equation is able to account for the inhomogeneous nature of the shock by using the surface- and volume-averaged undisturbed flow quantities, where "undisturbed flow" means what the flow would be without the particle present. The C-MRG model not only captures quasisteady drag effects but also the inviscid unsteady force by applying a time-history kernel to encode the effects of previous flow states on the current force. In the past, this model has been shown to capture the force of a shock passing over an isolated particle well in both air and water [40] at finite Mach numbers, although it does not attempt to take into account volume fraction. In the present work, we use the recent volume-fraction-corrected quasisteady model [11] along with the time-dependent effects of the shock passing over the particle as well as the neighbors within the C-MRG framework.

The behavior of drag force in an unsteady compressible flow is substantially different from that in the incompressible regime, and the difference is well captured by the C-MRG equation [38,39]. For instance, in the case of an isolated particle encountering rapid flow acceleration in the compressible regime, the inviscid unsteady force changes on the acoustic timescale, which is of the same order as the flow acceleration. Therefore, the inviscid unsteady force must be evaluated using a time-history kernel instead of being applied instantaneously as with the classical added mass force. Additionally, if the flow Mach number is sufficiently high, shocklets or bow shocks form, which induce inviscid drag [40]. Therefore, the effects of compressibility are significant and require detailed investigation.

The remainder of this paper is organized as follows. Section II outlines the computational approach and the specifics of the problem geometry and initial conditions. Section III includes a discussion of the flow fields in Sec. III A followed by a presentation of the drag force results in
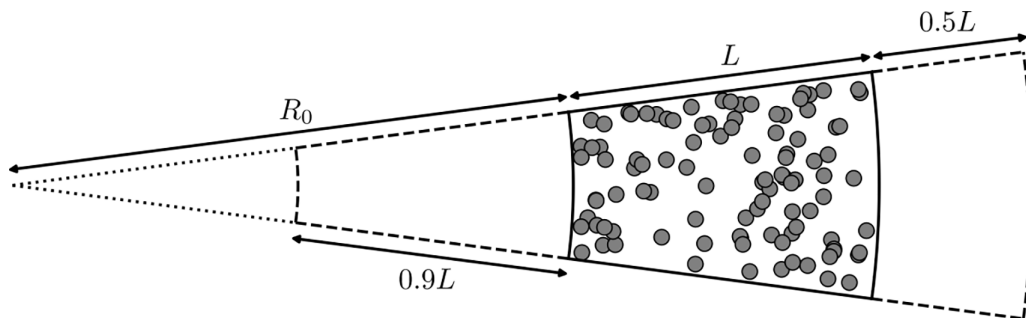
FIG. 1. Schematic of the simulation setup in cylindrical geometry. The dashed lines enclose the simulation domain, and the solid lines encircle the particle cloud.

Sec. III B comprising an outline of the C-MRG model in Sec. III B 1, a proposed model for the neighbor unsteady force in Sec. III B 3, and a comparison of the model to the particle-resolved (PR) results in Sec. III B 4. Finally, conclusions are drawn in Sec. IV.

II. METHODS

A. Governing equations

The following compressible Navier-Stokes equations govern the gas flow:

$$\frac{\partial \rho}{\partial t} + \vec{\nabla} \cdot (\rho \vec{u}) = 0, \tag{1}$$

$$\frac{\partial (\rho \vec{u})}{\partial t} + \vec{\nabla} \cdot (\rho \vec{u}\vec{u}) = -\vec{\nabla} p + \vec{\nabla} \cdot \boldsymbol{\sigma}, \tag{2}$$

and

$$\frac{\partial (\rho E)}{\partial t} + \vec{\nabla} \cdot (\rho E \vec{u} + p\vec{u}) = \vec{\nabla} \cdot (\boldsymbol{\sigma}\vec{u}) - \vec{\nabla} \cdot (\lambda \vec{\nabla} T), \tag{3}$$

where ρ is the density, $\vec{u}$ is the velocity, p is the pressure, λ is the thermal conductivity, and T is the temperature. The viscous stress tensor, $\boldsymbol{\sigma}$, is given by

$$\boldsymbol{\sigma} = \mu\big(\vec{\nabla}\vec{u} + (\vec{\nabla}\vec{u})^{\top} - \tfrac{2}{3}I\vec{\nabla} \cdot \vec{u}\big), \tag{4}$$

where μ is the dynamic viscosity, and I is the identity tensor. Additionally, the total energy per unit volume, E, is defined as

$$E = \rho e + \tfrac{1}{2}\rho \vec{u} \cdot \vec{u}, \tag{5}$$

where e is the internal energy per unit mass. An ideal gas is assumed with a constant ratio of specific heats of $\gamma = 1.4$. The Prandtl number is take to be a constant of 0.7. Finally, the viscosity is assumed to have a power-law dependence on temperature with an exponent of 0.76 [41]. These equations are solved using the code CHARLES from Cascade Technologies [42]. It uses third-order Runge-Kutta time marching paired with an entropy-stable scheme [43].

B. Problem specification

This work examines a cylindrically expanding shock passing through a stationary cloud of particles. The geometry of the domain is a section of a cylinder with a cloud of particles situated beyond a diaphragm which breaks and initializes a shock that travels outward through the particle bed. The domain is of radial length $2.4L$, where L is the radial extent of the particle bed situated $0.9L$ from the inner radius of the domain as shown in Fig. 1. The domain does not extend all the way to

TABLE I. Various cases considered.

Case	R_0/L	α_p	M_s	Re	Number of realizations	Number of particles
1	1.0	0.1	2.6	5000	5	1397
2	1.25	0.1	2.6	5000	3	1303
3	1.5	0.1	2.6	5000	3	1241
4	2.0	0.1	2.6	5000	5	1164
5	∞	0.1	2.6	5000	5	931

the center point of the cylinder. The inner boundary of the particle cloud is at radius R_0. The particle diameters and the cloud length are held constant at $D_p = 0.063$ mm and $L = 1.9$ mm, respectively. The arclength of the shell at the inner edge of the particle layer is held constant at $12.7D_p$ by varying the angular dimension. Additionally, the axial shell thickness is also a constant of $12.7D_p$. The shock is initialized via a discontinuity, where the driver section has an initial pressure of 3.6619 MPa and density of 12.508 kg/m^3. This discontinuity is located at a distance of $0.156L$ upstream of the particle cloud. This results in an initial shock Mach number, M_s, of 2.6. The Reynolds number, Re, is calculated using the initial postshock conditions and the particle diameter is approximately 5000. The radius of curvature, R_0, is varied while the particle volume fraction, α_p, is held constant at 0.1. An ensemble of simulations is performed with each realization consisting of a different random distribution of particles to increase the sample size in the evaluation of the ensemble average for better comparison with the drag models. The number of repeated simulations for the different cases is shown in Table I. Each simulation is fully three dimensional with a body-fitted grid resolving each particle.

The distribution of particles within the particle cloud is random with a minimum distance of $0.05D_p$ between particles. Given the geometry of the problem, it is convenient to define two different timescales. The first is the particle timescale denoted as $\tau = D_p/u_s$, where u_s is the shock velocity. Additionally, following Osnes *et al.* [44], the geometry allows for a second timescale related to the size of the particle cloud, $\tau_L = L/u_s$.

A body-fitted Voronoi grid was used to resolve the flow around each particle. The details of the body-fitted grid and the adequacy of grid resolution have been fully addressed in Refs. [44,45]. The grid resolution of all the simulations, whose particle force results are being analyzed in the present study, have been previously analyzed in Ref. [44], and found to be well converged with respect to Reynolds stress as shown in Fig. 2 of Ref. [44]. Additionally, using a slightly less refined grid, and the same computational method, Osnes *et al.* [45] observed the coefficient of drag on the particles to be converged for the corresponding planar case. These results establish the adequacy of grid resolution for the present investigation.

III. RESULTS AND FORCE MODELING

A. Flow fields

The flow fields may be summarized using average quantities which are denoted by $\langle \cdot \rangle$. These are spatial averages over the homogeneous angular and z directions. These are then averaged over multiple realizations for better convergence. The various cases exhibit remarkable similarity as we see from Fig. 2. Initially, the Mach number is zero throughout the domain and there is a pressure jump just upstream of the particle bed as displayed in Fig. 3, where the reference pressure, p_{ref}, is the initial postshock pressure. After the simulation begins, this pressure jump results in a shock that propagates downstream, steadily weakening due to the expanding geometry and the presence of the particles. The leading edge of the particle bed reflects a shock upstream after the initial shock interacts with the particles. The reflected shock then propagates upstream before reflecting off the inner boundary. The simulation ends prior to this reflected shock interacting with the particles again.
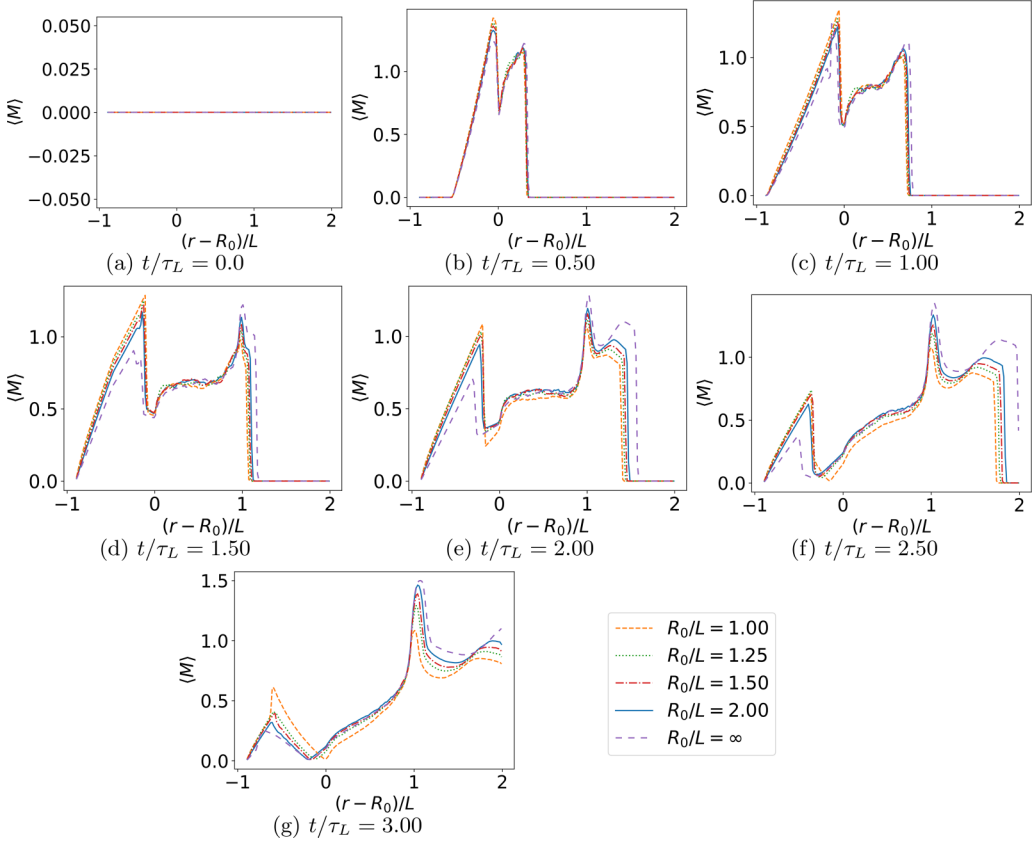
FIG. 2. Ensemble-averaged Mach number, $\langle M \rangle$, plotted as a function of scaled radius, $(r - R_0)/L$, at varying radii of curvature, R_0/L, at several times. $\tau_L = L/u_s$.

The primary shock travels through the particles and exits the particle bed at $(r - R_0)/L = 1$. At this outer edge of the particle bed, there is a peak in Mach number, and valleys in pressure and density as shown in Figs. 2–4 where the fluid is expanding as it exits the particle cloud. Here ρ_{ref} is the initial postshock density. These features of a peak in Mach number and a negative pressure gradient near the edge of the particle cloud result in higher drag for particles near the downstream edge of the cloud. In applications where particles move freely over a longer time, this will cause the particle cloud to expand radially as the particles near the rear edge move faster than particles near the front. Throughout the simulation, there is a positive radial Mach number gradient extending from the forward edge of the particle cloud to either the primary shock location before it exits the particle cloud or the rear edge of the particle cloud indicating a weakening postshock flow as exhibited by Fig. 2. At early times such as $t/\tau_L = 0.5$ shown in Fig. 2(b), this gradient is relatively steep and extends all the way to the forward edge of the particles, but as time progresses, such as at $t/\tau_L = 1.0$ displayed in Fig. 2(c), this gradient is localized to the neighborhood of the shock and the mean Mach number throughout the particle bed is relatively constant with minor fluctuations. Just after the shock has left the particle bed, at $t/\tau_L = 1.5$ exhibited in Fig. 2(d), the gradient becomes localized to the front and rear edges of the particle bed, but as time increases this gradient extends to the remainder of the particle bed as at $t/\tau_L = 3.0$ in Fig. 2(g).

Despite the notable similarities between cases, the radius of curvature plays a role in how the flow fields develop over time. For instance, the pressure plots at $t/\tau_L = 2.0$ in Fig. 3(e) exhibit a change in the pressure gradient with decreasing radius of curvature. This becomes clear as
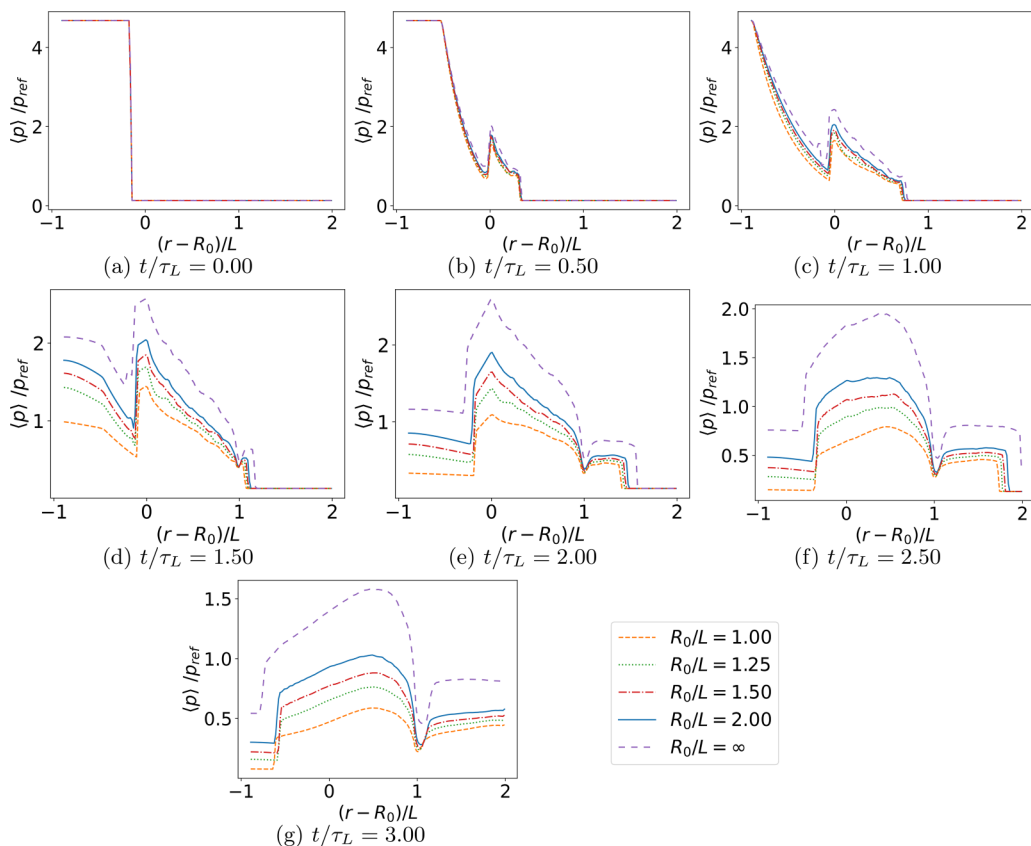
FIG. 3. Ensemble-averaged pressure, $\langle p \rangle$, plotted as a function of scaled radius, $(r - R_0)/L$, at varying radii of curvature, R_0/L, at several times. $\tau_L = L/u_s$. The reference pressure, p_{ref}, is the initial postshock pressure.

time progresses and the enhanced decay of the shock manifests for smaller radii of curvature in Figs. 3(d)–3(g). Similar features can also be seen in the density shown in Fig. 4. The Mach number also shows substantial differences with changing radius of curvature. One prominent feature that can be observed at $t/\tau_L = 2.0$ in Fig. 2(e) is that as the shock exits the particle bed it is stronger with decreasing radius of curvature. In the planar case shown in Fig. 2(e), the immediate postshock flow appears to be supersonic just upstream of the shock propagating at $(r - R_0)/L \approx 1.6$, whereas the postshock flow at a slightly upstream position in the $R_0/L = 1.0$ case is just below the sonic condition as exhibited in Fig. 2(e). Notice that in the high-curvature case the shock position is also slightly behind the shock position in the planar case, indicating that the shock velocity has decreased more in the $R_0/L = 1.0$ case than the planar case. This enhanced weakening of the shock in high-curvature environments is supported by the relative lowering of the postshock pressure and density with increasing curvature shown in Figs. 3 and 4. Note that these features continuously transition across intermediate levels of curvature.

Each of Figs. 2–4 represents an ensemble average of the flow across the multiple cases with differing realizations of uniformly random particle distributions of constant volume fraction as outlined in Table I. To examine the differences in the individual cases, Fig. 5 shows a comparison of the spatially averaged pressure fields for the various cases having $R_0/L = 1$. The ensemble averages of these cases are plotted in Figs. 2–4. Clearly, the variation between the cases in each realization is driven by the random particle distribution. The main features of the flow are not sensitive to this distribution and are therefore recovered in each case. The advantage of having
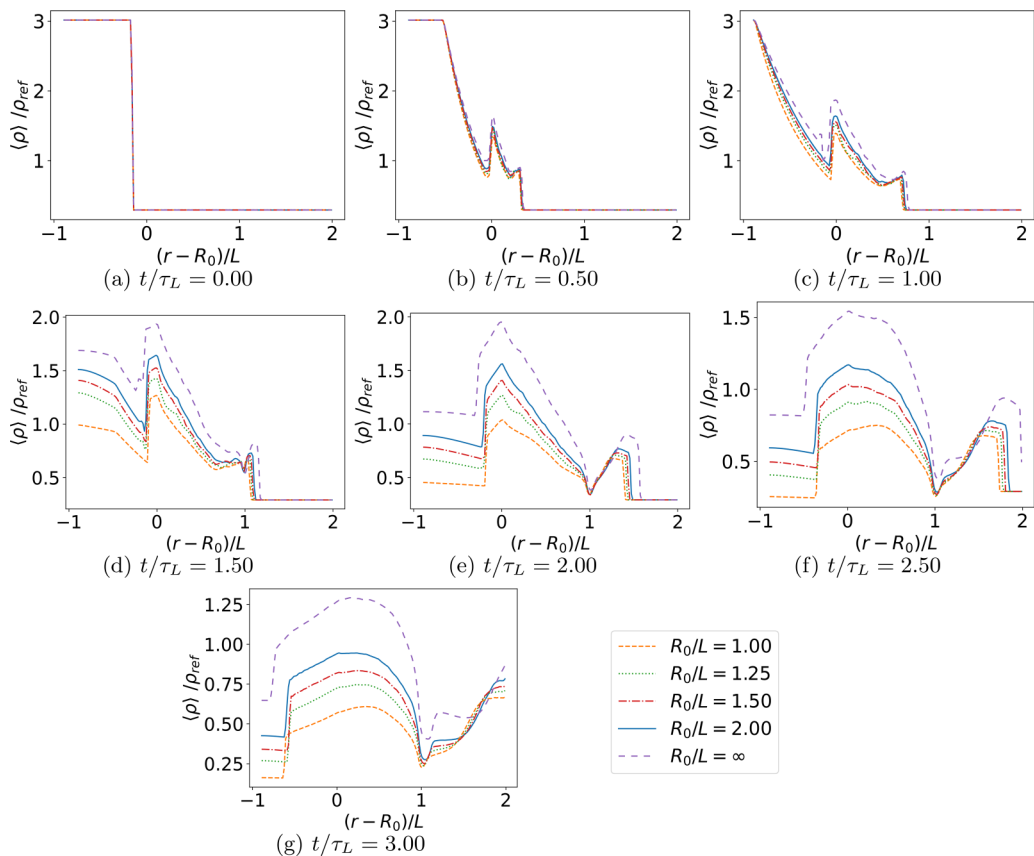
FIG. 4. Ensemble-averaged density, $\langle \rho \rangle$, plotted as a function of scaled radius, $(r - R_0)/L$, at varying radii of curvature, R_0/L, at several times. $\tau_L = L/u_s$. The reference density, ρ_{ref}, is the initial postshock density.

a large sample size for averaging is that drag as a function of radial position can be obtained statistically converged. Furthermore, a more converged approximation to the ensemble-averaged flow can be used to evaluate the drag models.

For a more detailed perspective of the general qualities shared across the various cases, the $R_0/L = 2.0$ case is observed in Fig. 6 where the Mach number has been plotted at several times. The common flow features, such as the shock propagating through the particle bed, the reflected wave propagating leftward back upstream, and the high Mach number near the rightward edge of the particles, are clear. However, additional detail beyond the average quantities can be observed, such as the development of pseudoturbulent wakes behind each particle as shown in Fig. 6 which intensify after the shock passes and form a complicated pattern of shocklets contributing to the inviscid drag on the particles. A detailed discussion of pseudoturbulence was presented by Osnes *et al.* [44].

B. Drag forces

1. C-MRG model

Reduced-order models of the forces experienced by particles are key for extending the microscale understanding derived from PR simulations to mesoscale EL simulations. Here, we compare our results to the C-MRG model [38,39]. This model extends to the compressible regime the pioneering work on incompressible flow by Maxey and Riley [46] and Gatignol [47]. Neglecting the viscous
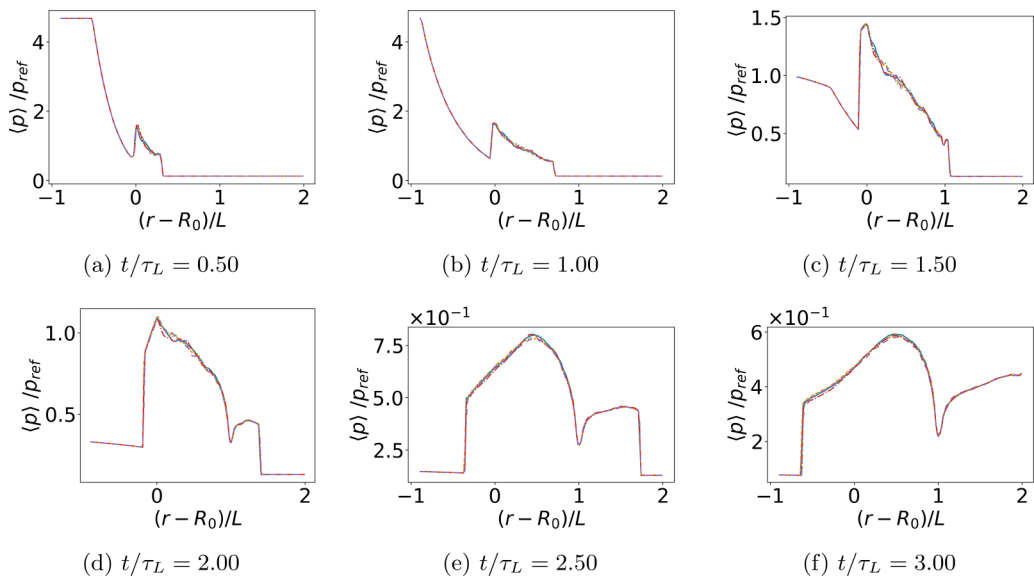
FIG. 5. Average (spatial, not ensemble) pressure plotted as a function of radius at several times for $R_0/L = 1.0$. The ensemble average of these make up some the results in Fig. 3. The only difference between cases is the particle distribution, which has the same volume fraction but a different microstructure. The initial condition has been omitted from this figure since the solutions are an exact match at that point. See Fig. 3 for the initial condition. The reference pressure, p_{ref}, is the initial postshock pressure. $\tau_L = L/u_s$.

unsteady term, the C-MRG model is given by

$$\vec{F}(t) = \underbrace{-S_p \overline{p_{un}\vec{n} + \boldsymbol{\sigma}\cdot\vec{n}}^S}_{\vec{F}_{un}} + \vec{F}_{qs} + \underbrace{3V_p \int_{-\infty}^{t} K_{iu}\left[\frac{\partial \overline{\rho_{un}\vec{u}_{un,r}}^S}{\partial t} + \overline{\vec{u}_{un}}^V \cdot \vec{\nabla}\overline{\rho_{un}\vec{u}_{un,r}}^S\right]_\xi d\xi}_{\vec{F}_{iu} = \vec{F}_{iu,l} + \vec{F}_{iu,nl}}, \quad (6)$$

where $\vec{F}$ is the force on the particle, the subscript *un* indicates an undisturbed quantity, S_p is the surface area of the particle, V_p is the volume of the particle, $\vec{n}$ is the outward pointing unit normal vector, $\overline{\cdot}^S$ denotes the surface average, $\overline{\cdot}^V$ denotes the volume average, K_{iu} is the inviscid unsteady kernel, and the subscript r indicates the radial component in the coordinate system of the particle,
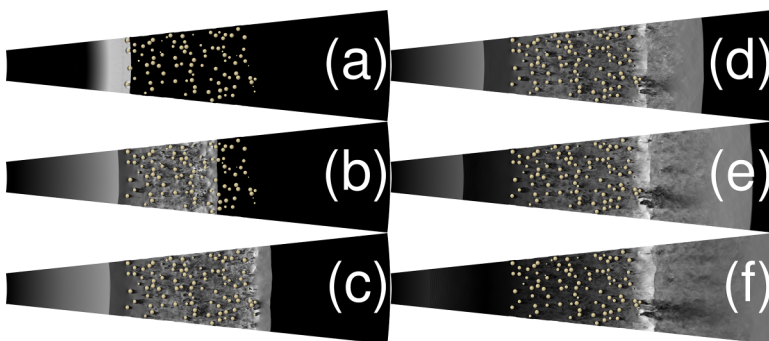

FIG. 6. Slice of Mach number for $R_0/L = 2.0$, plotted at t/τ_L values of (a) 0.20, (b) 0.96, (c) 1.51, (d) 2.00, (e) 2.49, and (f) 3.02.

such that for an arbitrary vector field, $\vec{w}$, $\vec{w}_r = (\vec{w} \cdot \vec{n})\vec{n}$. Here undisturbed flow of a particle is defined as that which would exist without that particle present, but in the presence of all other particles. The viscous unsteady force is neglected because it is not important in shock-particle interaction, especially at early times where excellent agreement has been shown between experiment and inviscid simulations [40]. At long times, quasisteady force becomes dominant and includes compressible inviscid effects as well as viscous effects. The undisturbed flow exerts the undisturbed force $\vec{F}_{un}$ on the particle, which can be directly calculated if the undisturbed flow is known. The quasisteady force, $\vec{F}_{qs}$, is the force that the particle will experience at long times under the current instantaneous conditions. In contrast, the inviscid unsteady force, which can be divided into linear and nonlinear components, $\vec{F}_{iu}$, is a generalization of the added mass force in compressible flows. A convolution integral with a time-history kernel is needed to take into account the finite speed of sound in a compressible flow.

In the linear limit, the inviscid unsteady kernel was analytically obtained by Parmar *et al.* [48], and extended empirically via a volume-averaged formulation by Behrendt *et al.* [30] to nonlinear conditions as

$$K_{iu}(t - \xi; \overline{M}^V) = (1 + 3.32\alpha_p) \frac{\bar{c}^V|_\xi}{R_p} \exp\left[-A \frac{(t-\xi)\bar{c}^V|_\xi}{R_p}\right] \cos\left[B \frac{(t-\xi)\bar{c}^V|_\xi}{R_p}\right], \qquad (7)$$

where c is the speed of sound, R_p is the particle radius, and M is the Mach number. Behrendt *et al.* [30] empirically found that in the subcritical regime of $0 < M < 0.6$, $A = 1.47M^2 - 0.23M + 1.00$, and $B = -1.74M^2 - 0.10M + 1.00$, thereby extending the zero Mach number limit of $A = B = 1$. Additionally, the first factor of $(1 + 3.32\alpha_p)$ is a volume fraction correction derived asymptotically in the dilute limit [49].

In the case of a single particle, the undisturbed flow is known analytically in the case of a shock passing over the particle, which can be used to calculate all the force contributions. In the presence of neighboring particles, the undisturbed flow of a particle is the flow that would exist in the absence of that particle, but in the presence of all other neighbors. Thus the true undisturbed flow of each particle will be slightly different due to the random arrangement of particles within the cloud. Here we do not have direct access to the undisturbed flow. Therefore, we instead use the averaged flow quantities $\langle\rho\rangle(r)$, $\tilde{u}_r(r)$, and $\langle p\rangle(r)$ as the undisturbed flow of a particle to evaluate the undisturbed flow force. This assumption is reasonable since there are many particles and thus removing one particle will not significantly modify the average flow. The quasisteady force is evaluated using the Reynolds number, Mach number, and volume-fraction-dependent correlation for the compressible flows presented by Osnes *et al.* [11]. This model is applied locally and then surface averaged as

$$\vec{F}_{qs} = \overline{\frac{1}{2} A_p \rho_{un} |\vec{u}_{un}| \vec{u}_{un} \Phi(M, \text{Re}, \alpha_p)}^S, \qquad (8)$$

where Φ is the volume-fraction-dependent drag correlation [11].

In order to evaluate the accuracy of the C-MRG model, we evaluate the model using the mean flow quantities obtained from the simulation and use them as the undisturbed quantities. The model results will be compared against the drag data obtained from the PR simulations postprocessed in the following manner. The particle bed is divided into 60 radial bins of width $W_b = L/60$ extending from the innermost particles (located close to $r = R_0$) to the outermost particles (located close to $r = R_0 + L$). The drag values on all the particles with a radial bin were averaged over all the realizations to approximate the ensemble average. The bin size was chosen as a compromise between two competing requirements. A narrow bin of small radial thickness would provide more accurate resolution of the ensemble-averaged flow information. On the other hand, a narrow bin size will require more realizations of random particle distributions to obtain a sufficiently converged ensemble-averaged flow. The present bin width is able to accurately capture the peak force, although the time duration of the peak is broadened somewhat due to the smearing of the ensemble-averaged flow properties.
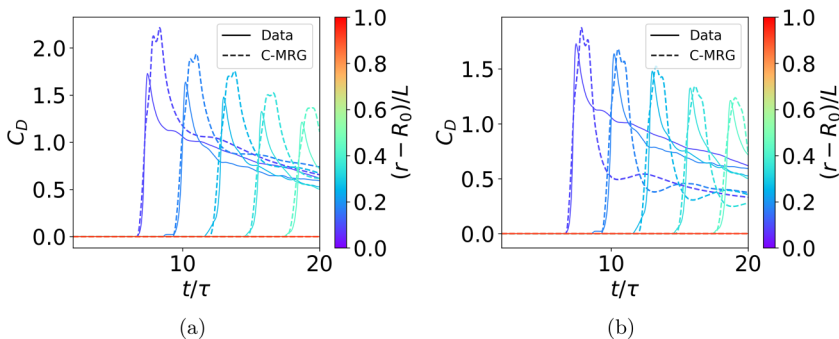
FIG. 7. C-MRG comparison to PR data without time delay (a) with volume fraction effects and (b) without volume fraction effects: $\Phi(M, \text{Re}, \alpha_p = 0)$. $R_0/L = 2.0$. Every fifth bin is shown here to make the plot easier to read.

For further analysis we neglect the particles that are within two particle diameters of the sidewalls. Prior to averaging, the drag data of each particle obtained from the PR simulations are shifted to align the initial peak location to match their shock arrival times. Also, the particles that are in the upstream- and downstream-most radial bins must be considered carefully when comparing with the quasisteady drag model of Ref. [11] since the particles in these bins are not completely surrounded on all sides by neighbors.

2. Preliminary comparison

Figures 7(a) and 7(b) show the early time comparison of bin-averaged drag force on the particles against two different versions of the C-MRG drag model. In Fig. 7(a) the quasisteady force term given in Eq. (8) is used with the volume fraction $\alpha_p = 0.1$, whereas in Fig. 7(b) the quasisteady force term was evaluated without the volume fraction correction by setting $\alpha_p = 0.0$. It is important to note that here and henceforth force evaluation using the C-MRG model (6) is always with all the force contributions (undisturbed flow force, quasisteady force, and inviscid unsteady force), unless otherwise stated. In Fig. 7, only the quasisteady term is varied by including volume fraction or not. Therefore, Fig. 7 exhibits the effect of including volume fraction effects in the quasisteady term, while including the other force contributions in the C-MRG model. We notice that in Fig. 7(a), the volume-fraction-corrected quasisteady drag causes the C-MRG model to overpredict the peak drag, but is reasonably accurate in capturing the postshock drag evolution. In contrast, in Fig. 7(b), the quasisteady drag of an isolated particle without the volume fraction correction within the C-MRG framework captures the peak drag quite well, but substantially underpredicts the postshock drag evolution. This suggests that the finite volume fraction correction does not apply during the initial interaction with the propagating primary shock. This observation seems reasonable considering the fact that the volume fraction effects are due to perturbation flow arising from the neighboring particles influencing the force on a particle. Clearly, during the interaction of the primary shock with a particle, only the perturbing effect of the particles directly upstream are felt. Since each particle is unaware of the presence of most of the neighbors to the side and downstream during this early interaction, including the volume fraction correction in the quasisteady drag is inappropriate. However, after the shock has passed, the perturbation effect of all the neighbors begins to influence the flow around a particle and comparison with the model that includes volume fraction effects in Fig. 7(a) is significantly better.

A more detailed plot of the peaks is shown in Fig. 8 where the peak force obtained for all the particles is plotted as a function of their streamwise location for case 4 ($R_0/L = 2$). The scatter plot shows the large number of particles used in approximating the ensemble average. Furthermore, the weakening of the shock as it propagated through the bed of particles is responsible for the steady
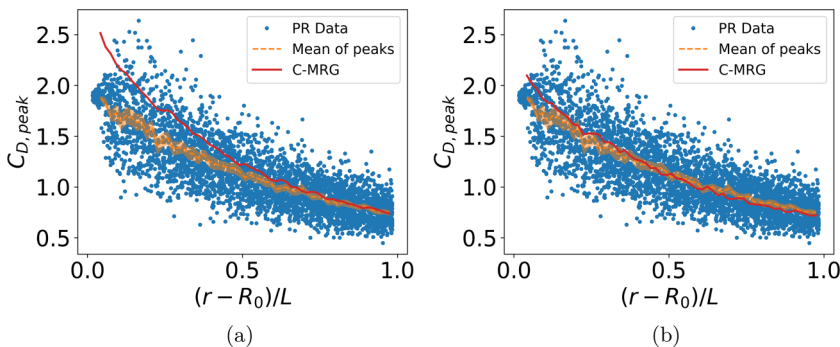
FIG. 8. C-MRG comparison of peak drag to PR data without time delay (a) with volume fraction effects and (b) without volume fraction effects: $\Phi(M, \text{Re}, \alpha_p = 0)$. $R_0/L = 2.0$. Note that while the C-MRG model includes all three force contributions (undisturbed flow, quasisteady, and inviscid unsteady), only the form of the quasisteady force changes between (a) and (b). The orange shading represents the 95% confidence interval for the PR data.

reduction in the peak drag force with increasing $(r - R_0)/L$. The mean drag force averaged over particles within each radial bin along with the 95% confidence interval is also shown in the figure as the orange-shaded region. Again in Fig. 8(a) we see that the peaks are substantially overpredicted when applying the volume fraction effects in the evaluation of the quasisteady force. As seen earlier, Fig. 8(b) shows that the peak force prediction substantially improves without the inclusion of volume fraction effect in the quasisteady force model.

3. Time-delayed volume fraction effect

Based on results presented in Figs. 7 and 8, it is clear that volume fraction effects should be carefully applied in high-speed compressible flows involving shock-particle interaction. The effect of neighboring particles must be based on the physical reasoning as to the delay in time a particle will experience the perturbation influence of its upstream, downstream, and lateral neighbors. When a shock wave approaches a particle surrounded by a random distribution of neighbors, in addition to the direct interaction of the shock as well as the postshock flow with the particle, perturbations arising from the interaction of the shock and the postshock flow with each neighbor will also play a role. But the influence of a neighbor is felt only in a delayed manner, since the perturbation flow of the neighbor initiates only upon the arrival of the shock wave at the neighbor and then that perturbation must also travel from the neighbor to the particle. Thus, the perturbation effect of lateral and downstream neighbors will be felt only after the passage of the initial shock past the particle and will not influence the peak drag force.

It must be noted that, had the flow in the neighborhood of the particle been time independent, then the perturbative effect of all the neighbors would also be time independent and the finite volume fraction quasisteady drag model presented in Eq. (8) will apply. Under unsteady conditions, when the flow seen by the neighbors is different from that of the reference particle (whose aerodynamic force modeling is being discussed), the volume fraction correction to quasisteady drag cannot be based solely on the instantaneous flow seen by the particle, due to the time-delayed effects described above. This effect is hitherto unexplored. It is an unsteady force contribution since it vanishes under steady conditions. The traditional added-mass (or inviscid unsteady) and Basset history (or viscous unsteady) forces given in Eq. (6) account for only the unsteady effects of the undisturbed flow "at the reference particle." Here we are interested in accounting for the unsteady flow seen by the neighbors in the volume fraction correction. In the following, we develop a model that accounts for the unsteady fluid-mediated particle-particle interaction. In principle, the C-MRG equation can account for the unsteady neighbor effects if the detailed undisturbed flow is known at

each particle. However, in an Euler-Lagrange context, the undisturbed flow of a particle is only known in an average sense such that the volume fraction effect is not resolved. The neighbor unsteady contribution is to properly account for the time-delayed application of the volume fraction effects.

Here we account for the time dependence of the volume fraction effect with an additional contribution to the force model, $\vec{F}_{nu}$, termed the unsteady (or time-dependent) neighbor force. This contribution is expected to be substantial only in the case of substantial variation in the mesoscale flow seen by the neighbors of a particle. In the case of a propagating shock, we expect some of the neighboring particles to be under preshock and others to be under postshock conditions, and more importantly, the distribution of pre- and postshock condition changes rapidly with time. Under nonshock conditions, we do not expect the particle-particle variation of the mesoscale flow to be large and therefore this additional contribution to the force model may not be important. With this argument, we seek a very simple empirical model of the form

$$\vec{F}_{nu} = -\vec{F}_{qs,\alpha} + \int_{-\infty}^{t} K_{nu}(t - \xi)\,\vec{F}_{qs,\alpha}\,d\xi, \tag{9}$$

where

$$\vec{F}_{qs,\alpha} = \overline{\tfrac{1}{2}A_p\rho_{un}|\vec{u}_{un}|\vec{u}_{un}\Phi(M, Re, \alpha_p)}^{S} - \overline{\tfrac{1}{2}A_p\rho_{un}|\vec{u}_{un}|\vec{u}_{un}\Phi(M, Re, \alpha_p = 0)}^{S} \tag{10}$$

is the quasisteady force difference with and without the finite volume fraction correction. Conceptually, the idea is to compensate for the initial premature inclusion of volume fraction effects in the quasisteady term. As the shock passes and acoustic waves are reflected from the neighboring particles to the reference particle, the volume fraction effects are applied gradually. At long times, this compensation is unnecessary and the model recovers to the quasisteady force with volume fraction effects, as the neighbor unsteady and inviscid unsteady forces approach zero. Therefore, the kernel encodes the distribution of acoustic wave arrival time from neighboring particles. We also need to enforce the condition

$$\int_{-\infty}^{t} K_{nu}(t - \xi)\,d\xi = 1, \tag{11}$$

in order to recover the long-time value of the correct quasisteady force with the volume fraction correction.

These requirements are easily satisfied by selecting a kernel based on an approximate probability density function (PDF) of arrival time of perturbation from surrounding neighbors. Here we select a log-normal distribution because of the qualitative behavior of having a peak at some point beyond zero followed by a decay,

$$K_{nu}(t - \xi) = \frac{1}{\beta_{nu}t_a} \frac{1}{[(t - \xi)/(\beta_{nu}t_a)]\sqrt{2\pi}} \exp\left[-\frac{(\ln\left[(t - \xi)/(\beta_{nu}t_a)\right])^2}{2}\right], \tag{12}$$

where β_{nu} is a fitting parameter, and t_a is an acoustic timescale. Additionally, the mean and variance of the corresponding normal distribution are set to 0 and 1, respectively. We propose a simple model for t_a based on a length scale, l, and the speed of sound,

$$t_a = \frac{l}{\overline{c}^V}. \tag{13}$$

The length scale is representative of the distance the perturbation must travel from the neighbor to arrive at the reference particle. We propose a model based on the following assumption,

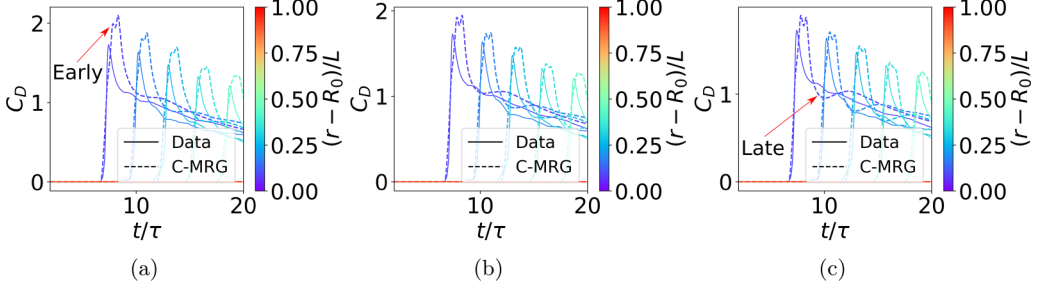$$\alpha_p^{1/3} = C_l \frac{D_p}{l + D_p}, \tag{14}$$

FIG. 9. C-MRG drag prediction compared to average PR data with the QS volume fraction delay kernel for $R_0/L = 2.0$ with (a) $\beta_{nu} = 1/3$, (b) $\beta_{nu} = 2/3$, and (c) $\beta_{nu} = 1$. Notice that for β_{nu} values too small, the volume fraction effects are applied too early, and for β_{nu} values too large, the volume fraction effects are applied too late.

which yields

$$l = D_p\left(C_l\alpha_p^{-1/3} - 1\right). \tag{15}$$

We use $C_l = 0.87$ to guarantee that $l > 0$ for the close random packed case of $\alpha_p = 0.65$. The constant β_{nu} remains to be determined. Figure 9 shows the model prediction for one of the cases considered for a few values of β_{nu}. Here, the coefficient of drag is defined in the usual way as

$$C_D = \frac{2F_r}{A_p\rho_{\text{ref}}u_{\text{ref}}^2}, \tag{16}$$

where F_r is the radial component of the force in the global cylindrical coordinates and u_{ref} is the initial postshock radial velocity. For $\beta_{nu} = 1/3$ shown in Fig. 9(a), the volume fraction effect is applied too early, resulting in an overprediction of peak drag. Conversely, in Fig. 9(c), for the larger value of $\beta_{nu} = 1$, the volume fraction effect is applied too late, resulting in a noticeable secondary dip. For $\beta_{nu} = 2/3$ as shown in Fig. 9(b) the agreement between the model prediction and the simulation results is reasonable. We emphasize that the above model, although motivated by physical reasoning, is empirical and involves significant uncertainty. Nevertheless, the model demonstrates a viable approach to capturing both the peak drag as well as the long-time behavior in a finite volume fraction compressible environment.

4. Comparison of the model to PR data

The C-MRG predictions of the drag history curves for all cases are compared to the bin-averaged drag data from the PR simulations in Fig. 10. The effect of the curvature is noticeable when comparing the $R_0/L = 1.0$ case in Fig. 10(a) to the planar ($R_0/L = \infty$) case in Fig. 10(e). Here, the latter peaks in the $R_0/L = 1.0$ case are much lower than those in the planar case as evidenced by comparing the peaks near $t/\tau = 40$ in Fig. 10. This is further evidenced by the plots of peak drag in Fig. 11 where we observe that the peak drag exhibits stronger decay for higher radii of curvature. In Fig. 11(f) the mean peaks are plotted for the various radii of curvature showing an enhanced peak decay due to increased radii of curvature. Additionally, the peak predictions appear to be best near the trailing edge of the particle bed where the prediction is often within the 95% confidence interval shown in Fig. 11. The 95% confidence interval refers to the confidence interval for the mean drag calculated directly from the PR data presented in this work. The small overprediction of peaks at the early part of the particle bed is a limitation of the current model. It is also worth noting that the peak predicted with the model is somewhat wider than the PR data; however, this seems to be the case with or without inclusion of the neighbor unsteady force (compare Figs. 10 and 9) regardless of the choice of β. This error in prediction will greatly decrease when the PR fluid flow data finely resolve the shock structure as in the work of Behrendt *et al.* [40]. Therefore, the wider peak predicted
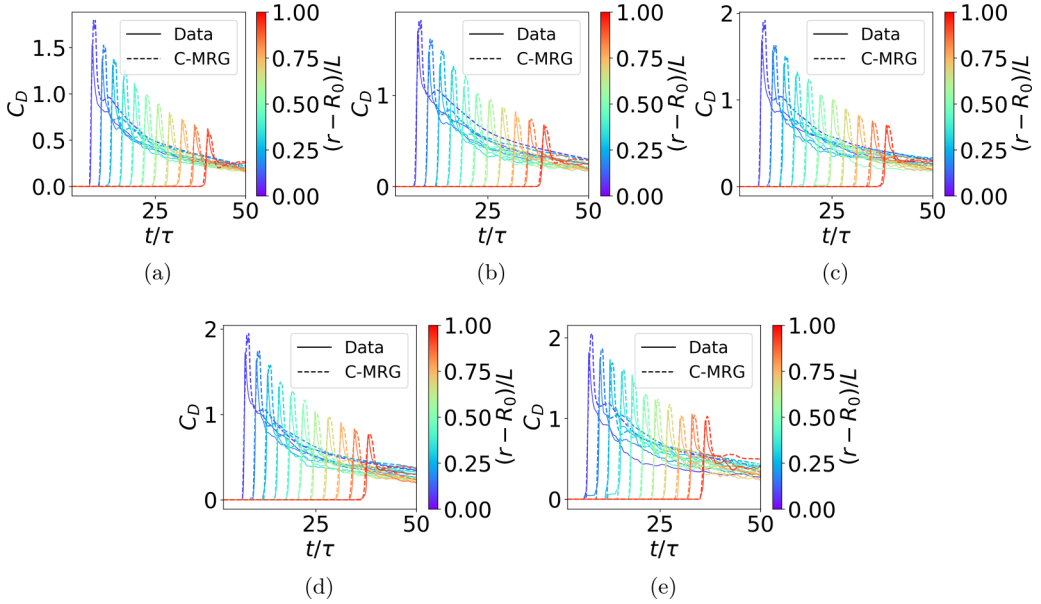
FIG. 10. C-MRG drag prediction comparison to PR for early to intermediate times for (a) $R_0/L = 1.0$, (b) $R_0/L = 1.25$, (c) $R_0/L = 1.5$, (d) $R_0/L = 2.0$, and (e) $R_0/L = \infty$. Every fifth bin is shown for clarity.
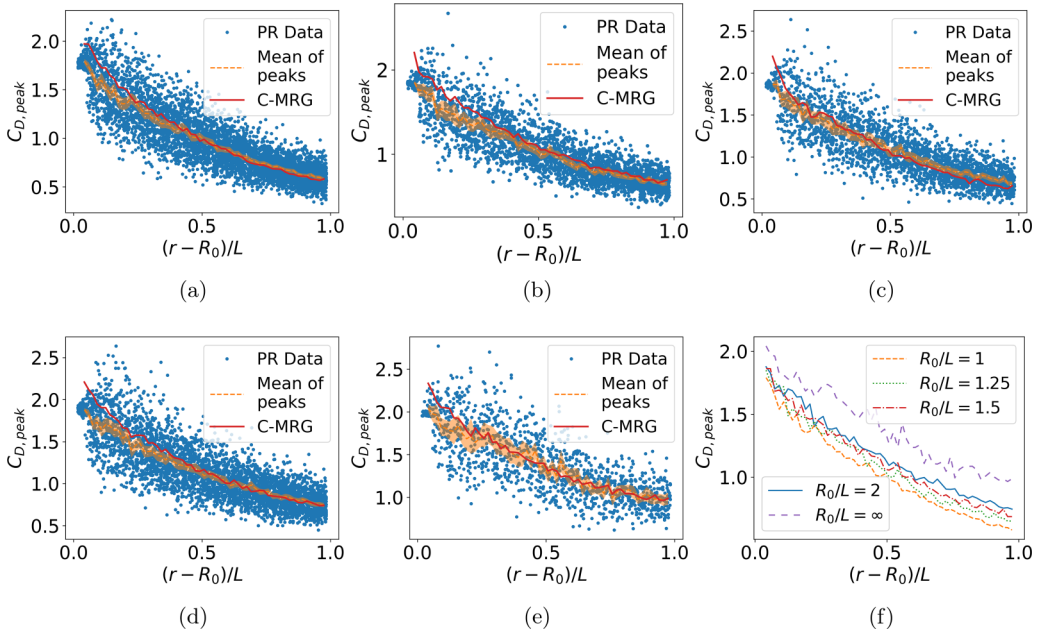

FIG. 11. Peak drag for the C-MRG prediction compared to the PR data plotted with its mean for (a) $R_0/L = 1.0$, (b) $R_0/L = 1.25$, (c) $R_0/L = 1.5$, (d) $R_0/L = 2.0$, and (e) $R_0/L = \infty$. The bounds surrounding the mean PR values indicate the 95% confidence interval. (f) A comparison of the mean peaks from the other plots to highlight the effect of curvature.
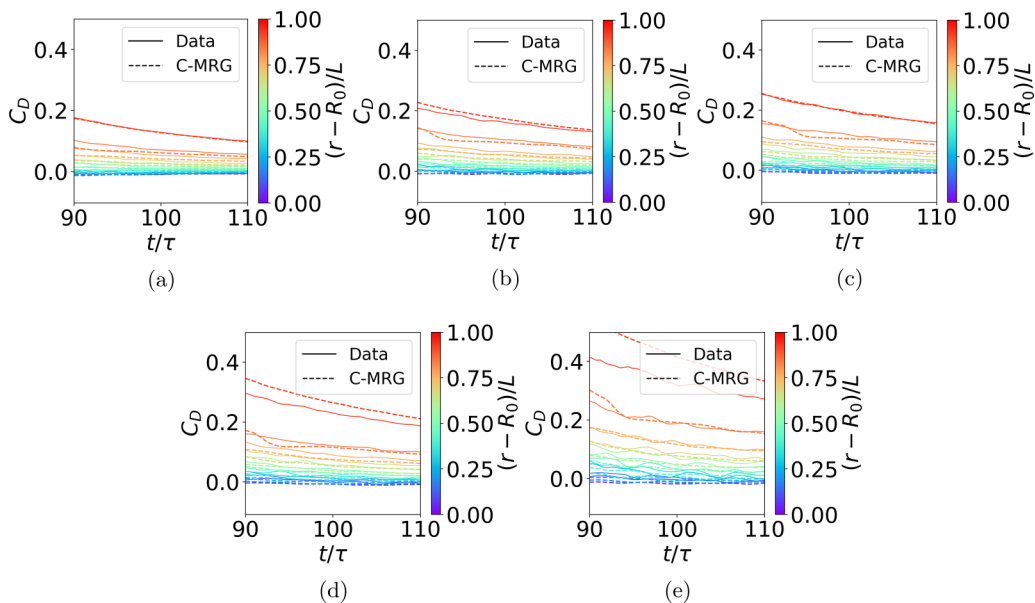
FIG. 12. Long-time drag comparison for the C-MRG prediction compared to the PR data plotted with its mean for (a) $R_0/L = 1.0$, (b) $R_0/L = 1.25$, (c) $R_0/L = 1.5$, (d) $R_0/L = 2.0$, and (e) $R_0/L = \infty$. Every fifth bin is shown for clarity.

here is due to the coarse resolution of the bin-averaged flow data. As a result, in the evaluation of the C-MRG equation, the shock is effectively not sharp.

As can be seen in Fig. 10, the model overpredicts the drag for particles near the front of the particle bed at intermediate times after the shock passage. For example, in Fig. 10(b), we clearly see the C-MRG prediction for the first particle is still somewhat higher than the bin-averaged drag from the PR simulations at $t/\tau = 50$. This overprediction of drag at early times is not due to the quasisteady component since we see an excellent match of the quasisteady force at late times after transient effects have diminished as displayed in Fig. 12. This figure shows a comparison of the quasisteady model prediction (dashed lines) against the bin-averaged simulation data (solid lines) for every fifth bin as a function of time. The agreement is quite good and offers additional support for the Reynolds number, Mach number, and volume-fraction-dependent compressible quasisteady drag model presented by Osnes *et al.* [11]. For the downstream half of the particle bed, whose force remains substantial during the time period of investigation, we observe the model prediction to be generally very good and within the error bounds.

The downstream motion of the particles depends on the time-integrated force (or impulse) on the particles. Here we define the aerodynamic impulse on a particle as

$$I(t/\tau) = \frac{1}{\tau} \int_0^t C_D dt. \tag{17}$$

The resultant impulse at $t/\tau = 100$ for all the particles is presented as a scatter plot in Fig. 13 as a function of the particle's normalized radial location. Near the rear of the particle bed there is a significant increase in impulse due to the substantial rise in Mach number shown in Fig. 2, and strong negative pressure gradient displayed in Fig. 3. In this region, the C-MRG model captures the impulse adequately. However, for the cases shown in Figs. 13(c) and 13(d), the impulse is substantially overpredicted in the upstream third of the particle bed. Again, this overprediction is likely not due to the quasisteady drag model because, at late times when the unsteady terms are negligible, the QS drag prediction is excellent as exhibited by Fig. 12.
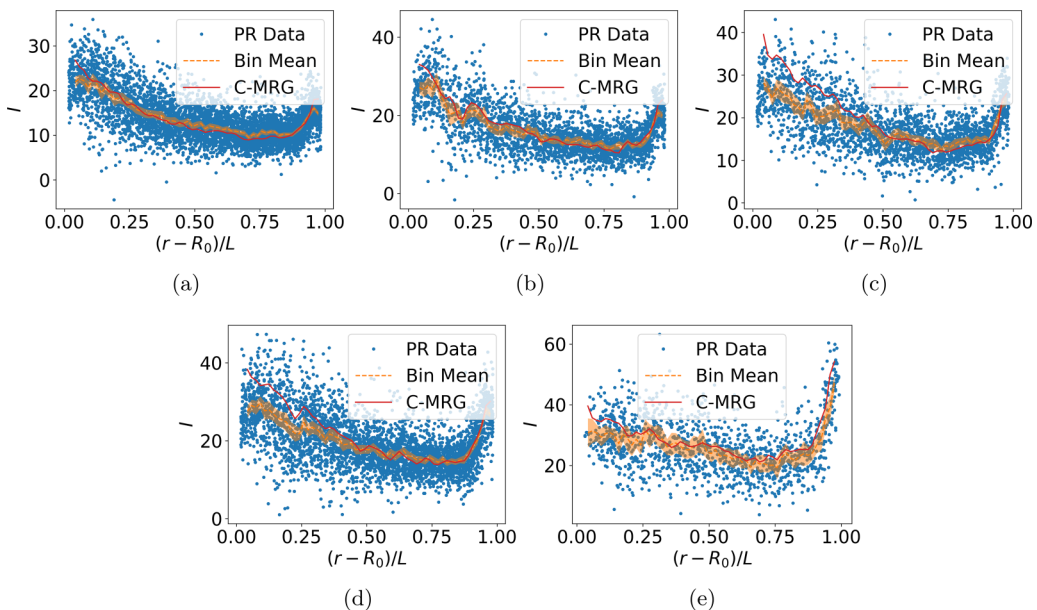
FIG. 13. Long-time impulse at $t/\tau = 100$ for the C-MRG prediction compared to the PR data plotted with its mean for (a) $R_0/L = 1.0$, (b) $R_0/L = 1.25$, (c) $R_0/L = 1.5$, (d) $R_0/L = 2.0$, and (e) $R_0/L = \infty$. The bounds surrounding the mean PR values indicate the 95% confidence interval.

The late-time agreement presented in Fig. 12 suggests the accuracy of the quasisteady model presented in Ref. [11] for the present cylindrical configuration. As a result, the difference observed in the model prediction at intermediate time is likely due to the limitations of the inviscid unsteady force. The quasisteady force, by itself, is appropriate only when the postshock flow reaches its final value and the pseudoturbulent wakes fully develop. In the intermediate time before this occurs, the inviscid unsteady force must account for the transient nature of the evolving wake. To examine these contributions, the components of the force model are shown in Fig. 14, where the inviscid unsteady force and the undisturbed forces rise first as the shock passes and then decline sharply. The inviscid unsteady force then becomes negative, which has been observed by others [50,51] and remains negative but low in magnitude for some time. It remains nearly zero as time continues. Based on the present comparison it can be argued that an improved version of the inviscid unsteady force is needed to more accurately capture the force dynamics at intermediate times while the turbulent wake is developing after the shock has passed in multiparticle systems.

To highlight the importance of accurate modeling of Reynolds number, Mach number, and volume-fraction-dependent quasisteady drag, and the unsteady forces, as an example we compare with the performance of the force model of Boiko *et al.* [52] that was used in the simulations by Jacobs *et al.* [53] to predict a shock interacting with a particle cloud. This force model (termed the QS-PG model) only includes the quasisteady and pressure gradient terms, neglecting the inviscid unsteady term as well as the volume fraction effects in the quasisteady contribution. Additionally, the model treats the particles as point particles instead of using surface and volume averaging as in the C-MRG equation. The PR results averaged over radial bins are compared with the QS-PG model prediction in Fig. 15. The QS-PG model leads to substantial error at early times where the peak drag is not captured well because the inviscid unsteady force is neglected as displayed in Fig. 15(b). Additionally, the pressure gradient force is diminished at early times since the filter width is substantially larger than a single particle. At late times, when the volume fraction effects are significant, the model also substantially underpredicts drag because this effect is neglected. This also leads to an underprediction of impulse as illustrated in Fig. 15(c). Therefore, the volume
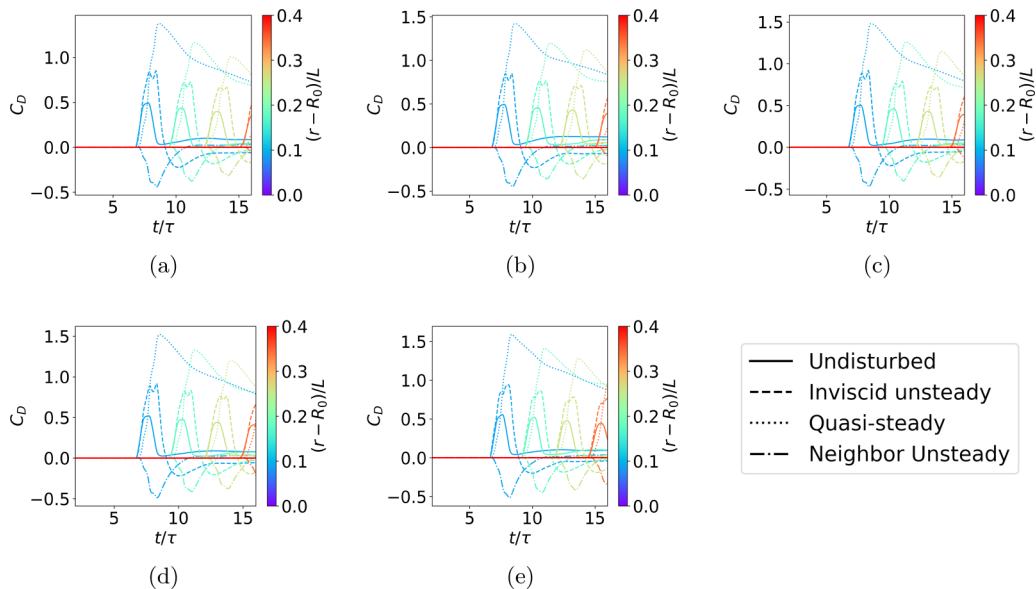
FIG. 14. C-MRG prediction components compared to the PR data plotted with its mean for (a) $R_0/L = 1.0$, (b) $R_0/L = 1.25$, (c) $R_0/L = 1.5$, (d) $R_0/L = 2.0$, and (e) $R_0/L = \infty$. Every fifth bin is shown for clarity.

fraction effects are very important when the long-time impulse is desired. Additionally, the inviscid unsteady and neighbor unsteady terms become important when accuracy is desired as the shock passes over the particles.

IV. CONCLUSION

The ability to accurately model the time-dependent force on a particle subjected to a time-varying flow is of fundamental interest in Euler-Lagrange computations of particle-laden flows. The modeling task becomes far more complicated when the particle is surrounded by a random distribution of neighboring particles. The average influence of neighbors is traditionally included in terms of a volume fraction correction to the quasisteady drag and also to the added mass or inviscid unsteady force. The volume fraction correction is intended to account for the perturbation flow induced on a particle due to the presence of neighbors and as the local volume fraction tends to zero, perturbation due to neighbors approaches zero, as does the volume fraction correction. The quasisteady drag is
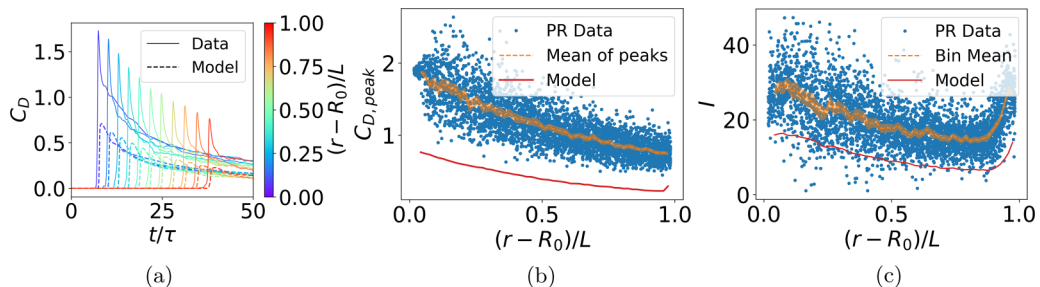

FIG. 15. Drag model used by Jacobs et al. [53] for shock-particle interaction compared to the present particle-resolved data for $R_0/L = 2$. The plots are comparisons of (a) time history of drag, (b) peak drag as a function of position, and (c) long-time impulse ($t/\tau = 100$) as a function of position.

calculated on the assumption that the undisturbed flow of the particle that existed at the time of evaluation of the force existed for a long time. In applying the volume fraction correction it is also assumed that the undisturbed flow of the particle applies at all the neighboring particles.

The key finding of this work is the realization that, under unsteady conditions at finite volume fraction, there must be an additional force contribution to account for the fact that the flow seen by the neighbors may not be the same as that of the reference particle whose force is being evaluated. This contribution is particularly important in compressible flows under conditions of shock propagation, where, as the shock propagates over the reference particle, many of the reference particle's lateral and downstream neighbors are still immersed in the preshock quiescent condition and do not contribute to neighbor-induced perturbation at the particle. Thus, evaluating the quasisteady force using the Reynolds number, Mach number, and volume-fraction-dependent drag correlation of Ref. [11] overpredicts the peak drag during the early period of shock-particle interaction. This overprediction is due to the finite volume fraction correction, since the shock has not reached most of the downstream neighbors and the perturbation of many others has not yet reached the reference particle due to finite speed of propagation. It is observed that the peak drag of each particle can be better predicted ignoring the volume fraction effect and computing the quasisteady force as that of an isolated particle. On the other hand, after the shock has propagated several diameters downstream, the long-time evolution of the force is well predicted with the finite volume fraction correction of Ref. [11]. That is, once the shock propagates over all the surrounding neighbors and their perturbation flows propagate back to influence the reference particle, the finite volume fraction effect is fully realized. Here we present a simple model for the unsteady effect of neighbors, $\vec{F}_{nu}$, which in conjunction with the quasisteady force model (8) offers a good representation of the particle force obtained in particle-resolved simulations.

The PR simulations of shocks in expanding cylindrical geometry were used to capture much of the three-dimensional physics associated with random arrays of particles. Unlike planar shock tube simulations, the shock strength decayed as it progressed through the particle bed due to both the presence of the particles and the expanding nature of the geometry. These viscous simulations provided accurate drag data for each particle in the cloud, allowing for comparison to the C-MRG model. The C-MRG model appears to work as well in cylindrical geometry as in planar geometry since the radii of curvature were much larger than the particle diameter. The key finding was that a neighbor-induced unsteady force must be included if peak drag is to be predicted accurately in the presence of neighbors. When including volume fraction dependence in the quasisteady term only, the C-MRG model compares favorably to simpler models in the literature with respect to prediction of long-term impulse. However, even with this improved formulation, the inviscid unsteady and neighbor unsteady forces must be included to accurately capture the significant transient peak in drag that occurs as the shock passes.

[1] F. Bashforth, *Reports on Experiments Made with the Bashforth Chronograph to Determine the Resistance of the Air to the Motion of Projectiles, 1865-1870* (Her Majesty's Stationery Office, London, 1870).

[2] J. Capecelatro and J. Wagner, Gas-particle dynamics in high-speed flows, Annu. Rev. Fluid Mech. **56**, 379 (2024).

[3] G. G. Stokes *et al.*, On the effect of the internal friction of fluids on the motion of pendulums (1851).

[4] S. Ganguli and S. K. Lele, Drag of a heated sphere at low Reynolds numbers in the absence of buoyancy, J. Fluid Mech. **869**, 264 (2019).

[5] J. Horwitz and A. Mani, Accurate calculation of Stokes drag for point-particle tracking in two-way coupled flows, J. Comput. Phys. **318**, 85 (2016).

[6] R. Clift, J. R. Grace, and M. E. Weber, *Bubbles, Drops, and Particles* (Dover Publications, Inc. Mineola, NY, 2005).

[7] C. T. Crowe, J. D. Schwarzkopf, M. Sommerfeld, and Y. Tsuji, *Multiphase Flows with Droplets and Particles* (CRC Press, Boca Raton, FL, 2011).

[8] E. Loth, Compressibility and rarefaction effects on drag of a spherical particle, AIAA J. **46**, 2219 (2008).

[9] E. Loth, J. T. Daspit, M. Jeong, T. Nagata, and T. Nonomura, Supersonic and hypersonic drag coefficients for a sphere, AIAA J. **59**, 3261 (2021).

[10] M. Khalloufi and J. Capecelatro, Drag force of compressible flows past random arrays of spheres, Int. J. Multiphase Flow **165**, 104496 (2023).

[11] A. N. Osnes, M. Vartdal, M. Khalloufi, J. Capecelatro, and S. Balachandar, Comprehensive quasi-steady force correlations for compressible flow through random particle suspensions, Int. J. Multiphase Flow **165**, 104485 (2023).

[12] A. M. Milne, C. Parrish, and I. Worland, Dynamic fragmentation of blast mitigants, Shock Waves **20**, 41 (2010).

[13] K. Balakrishnan and S. Menon, On turbulent chemical explosions into dilute aluminum particle clouds, Combust. Theory Model. **14**, 583 (2010).

[14] F. Graf, E. Meiburg, and C. Haertel, Density-driven instabilities of miscible fluids in a hele-shaw cell: Linear stability analysis of the three-dimensional stokes equations, J. Fluid Mech. **451**, 261 (2002).

[15] R. B. Koneru, B. Rollin, B. Durant, F. Ouellet, and S. Balachandar, A numerical study of particle jetting in a dense particle bed driven by an air-blast, Phys. Fluids **32**, 093301 (2020).

[16] F. Ouellet, B. Rollin, R. Koneru, J. Garno, and S. Balachandar, Effects of perturbing the particle volume fraction distribution in blast-driven multiphase instability, Shock Waves **31**, 337 (2021).

[17] A. M. Lattanzi, V. Tavanashad, S. Subramaniam, and J. Capecelatro, Stochastic model for the hydrodynamic force in Euler-Lagrange simulations of particle-laden flows, Phys. Rev. Fluids **7**, 014301 (2022).

[18] S. Tenneti, R. Garg, and S. Subramaniam, Drag law for monodisperse gas-solid systems using particle-resolved direct numerical simulation of flow past fixed assemblies of spheres, Int. J. Multiphase Flow **37**, 1072 (2011).

[19] G. Akiki, T. L. Jackson, and S. Balachandar, Pairwise interaction extended point-particle model for a random array of monodisperse spheres, J. Fluid Mech. **813**, 882 (2017).

[20] Y. Mehta, C. Neal, K. Salari, T. L. Jackson, S. Balachandar, and S. Thakur, Propagation of a strong shock over a random bed of spherical particles, J. Fluid Mech. **839**, 157 (2018).

[21] S. S. Hsiao, K. Salari, and S. Balachandar, Compressible pairwise interaction extended point-particle model for force prediction of shock-particle bed interaction, Phys. Rev. Fluids **8**, 054301 (2023).

[22] B. Siddani, S. Balachandar, W. C. Moore, Y. Yang, and R. Fang, Machine learning for physics-informed generation of dispersed multiphase flow using generative adversarial networks, Theor. Comput. Fluid Dyn. **35**, 807 (2021).

[23] B. Siddani and S. Balachandar, Point-particle drag, lift, and torque closure models using machine learning: Hierarchical approach and interpretability, Phys. Rev. Fluids **8**, 014303 (2023).

[24] Y. Ling, J. L. Wagner, S. J. Beresh, S. P. Kearney, and S. Balachandar, Interaction of a planar shock wave with a dense particle curtain: Modeling and experiments, Phys. Fluids **24**, 113301 (2012).

[25] J. L. Wagner, S. J. Beresh, S. P. Kearney, B. O. M. Pruett, and E. K. Wright, Shock tube investigation of quasi-steady drag in shock-particle interactions, Phys. Fluids **24**, 123301 (2012).

[26] O. Sen, N. J. Gaul, K. Choi, G. Jacobs, and H. Udaykumar, Evaluation of kriging based surrogate models constructed from mesoscale computations of shock interaction with particles, J. Comput. Phys. **336**, 235 (2017).

[27] E. P. DeMauro, J. L. Wagner, S. J. Beresh, and P. A. Farias, Unsteady drag following shock wave impingement on a dense particle curtain measured using pulse-burst PIV, Phys. Rev. Fluids **2**, 064301 (2017).

[28] Z. Hosseinzadeh-Nik, S. Subramaniam, and J. D. Regele, Investigation and quantification of flow unsteadiness in shock-particle cloud interaction, Int. J. Multiphase Flow **101**, 186 (2018).

[29] A. N. Osnes, M. Vartdal, M. G. Omang, and B. A. P. Reif, Particle-resolved simulations of shock-induced flow through particle clouds at different Reynolds numbers, Phys. Rev. Fluids **5**, 014305 (2020).

[30] J. Behrendt, S. Balachandar, and T. P. McGrath, Shock interacting with a random array of stationary particles underwater, Phys. Rev. Fluids **7**, 023401 (2022).

[31] V. Boniou and R. O. Fox, Shock–particle-curtain-interaction study with a hyperbolic two-fluid model: Effect of particle force models, Int. J. Multiphase Flow **169**, 104591 (2023).

[32] F. Zhang, D. Frost, P. Thibault, and S. Murray, Explosive dispersal of solid particles, Shock Waves **10**, 431 (2001).

[33] D. L. Frost, Y. Grégoire, O. Petel, S. Goroshin, and F. Zhang, Particle jet formation during explosive dispersal of solid particles, Phys. Fluids **24**, 091109 (2012).

[34] Q. Pontalier, J. Loiseau, S. Goroshin, and D. L. Frost, Experimental investigation of blast mitigation and particle-blast interaction during the explosive dispersal of particles and liquids, Shock Waves **28**, 489 (2018).

[35] D. L. Frost, Heterogeneous/particle-laden blast waves, Shock Waves **28**, 439 (2018).

[36] K. T. Hughes, S. Balachandar, A. Diggs, R. Haftka, N. H. Kim, and D. Littrell, Simulation-driven design of experiments examining the large-scale, explosive dispersal of particles, Shock Waves **30**, 325 (2020).

[37] M. Gomez, D. K. Lauriola, M. N. Slipchenko, S. Roy, S. F. Son, and T. R. Meyer, Spatiotemporally resolved 5-MHz visualization and particle image velocimetry in early time multiphase blasts, Optics Lasers Eng. **161**, 107351 (2023).

[38] M. Parmar, A. Haselbacher, and S. Balachandar, Equation of motion for a sphere in non-uniform compressible flows, J. Fluid Mech. **699**, 352 (2012).

[39] S. Annamalai and S. Balachandar, Faxén form of time-domain force on a sphere in unsteady spatially varying viscous compressible flows, J. Fluid Mech. **816**, 381 (2017).

[40] J. Behrendt, S. Balachandar, J. Garno, and T. P. McGrath, Modeling of shock-induced force on an isolated particle in water and air, Phys. Fluids **34**, 016108 (2022).

[41] F. S. Sherman, A low-density wind-tunnel study of shock-wave structure and relaxation phenomena in gases, Technical report No. NACA-TN-3298 (NASA, USA, 1955), https://ntrs.nasa.gov/citations/19930084209.

[42] G. A. Bres, S. T. Bose, M. Emory, F. E. Ham, O. T. Schmidt, G. Rigas, and T. Colonius, Large-eddy simulations of co-annular turbulent jet using a Voronoi-based mesh generation framework, in *2018 AIAA/CEAS Aeroacoustics Conference* (AIAA, Reston, VA, 2018), p. 3302.

[43] M. Masquelet, J. Yan, A. Dord, G. Laskowski, L. Shunn, L. Jofre, and G. Iaccarino, Uncertainty quantification in large eddy simulations of a rich-dome aviation gas turbine, in *ASME Turbo Expo 2017: Turbomachinery Technical Conference and Exposition* (American Society of Mechanical Engineers, New York, 2017), pp. V04BT04A049–V04BT04A049.

[44] A. N. Osnes, M. Vartdal, M. G. Omang, and B. A. P. Reif, Numerical investigation of shock wave particle cloud interaction in cylindrical geometries, in *Proceedings of the 10th National Conference on Computational Mechanics (MekIT 19), Trondheim, Norway* (NTNU, 2019), pp. 1–25.

[45] A. N. Osnes, M. Vartdal, M. G. Omang, and B. A. P. Reif, Computational analysis of shock-induced flow through stationary particle clouds, Int. J. Multiphase Flow **114**, 268 (2019).

[46] M. R. Maxey, Equation of motion for a small rigid sphere in a nonuniform flow, Phys. Fluids **26**, 883 (1983).

[47] R. Gatignol, The Faxen formulae for a rigid particle in an unsteady non-uniform stokes flow, J. Mec. Theor. Appl. **2**, 143 (1983).

[48] M. Parmar, A. Haselbacher, and S. Balachandar, Generalized Basset-Boussinesq-Oseen equation for unsteady forces on a sphere in a compressible flow, Phys. Rev. Lett. **106**, 084501 (2011).

[49] A. Biesheuvel and S. Spoelstra, The added mass coefficient of a dispersion of spherical gas bubbles in liquid, Int. J. Multiphase Flow **15**, 911 (1989).

[50] M. Sun, T. Saito, K. Takayama, and H. Tanno, Unsteady drag on a sphere by shock wave loading, Shock Waves **14**, 3 (2005).

[51] M. Parmar, A. Haselbacher, and S. Balachandar, On the unsteady inviscid force on cylinders and spheres in subcritical compressible flow, Philos. Trans. R. Soc. A **366**, 2161 (2008).

[52] V. M. Boiko, V. P. Kiselev, S. P. Kiselev, A. N. Papyrin, S. V. Poplavsky, and V. M. Fomin, Shock wave interaction with a cloud of particles, Shock Waves **7**, 275 (1997).

[53] G. B. Jacobs, W. S. Don, and T. Dittmann, High-order resolution Eulerian-Lagrangian simulations of particle dispersion in the accelerated flow behind a moving shock, Theor. Comput. Fluid Dyn. **26**, 37 (2012).